

Urease-powered nanomotor containing STING agonist for bladder cancer immunotherapy

Received: 23 March 2023

Accepted: 6 November 2024

Published online: 15 November 2024



Hyunsik Choi^{1,2,9}, Seung-hwan Jeong^{3,4,9}, Cristina Simó⁵, Anna Bakenecker¹, Jordi Liop⁵, Hye Sun Lee⁴, Tae Yeon Kim⁶, Cheol Kwak^{3,4}✉, Gou Young Koh⁷✉, Samuel Sánchez^{1,8}✉ & Sei Kwang Hahn^{2,6}✉

Most non-muscle invasive bladder cancers have been treated by transurethral resection and following intravesical injection of immunotherapeutic agents. However, the delivery efficiency of therapeutic agents into bladder wall is low due to frequent urination, which leads to the failure of treatment with side effects. Here, we report a urease-powered nanomotor containing the agonist of stimulator of interferon genes (STING) for the efficient activation of immune cells in the bladder wall. After characterization, we perform in vitro motion analysis and assess in vivo swarming behaviors of nanomotors. The intravesical instillation results in the effective penetration and retention of nanomotors in the bladder. In addition, we confirm the anti-tumor effect of nanomotor containing the STING agonist (94.2% of inhibition), with recruitment of CD8⁺ T cells (11.2-fold compared with PBS) and enhanced anti-tumor immune responses in bladder cancer model in female mice. Furthermore, we demonstrate the better anti-tumor effect of nanomotor containing the STING agonist than those of the gold standard Bacille Calmette-Guerin therapy and the anti-PD-1 inhibitor pembrolizumab in bladder cancer model. Taken together, the urease-powered nanomotor would provide a paradigm as a next-generation platform for bladder cancer immunotherapy.

Bladder cancer is the fourth most common cancer in men worldwide and the incidence of bladder cancer is gradually increasing with aging^{1,2}. As a representative symptom of bladder cancer, hematuria allows the early detection of bladder cancer and almost 75% of bladder cancers are diagnosed as a non-muscle invasive bladder cancer (NMIBC)³. The current primary treatment for NMIBC involves the transurethral resection of bladder tumors, followed by the intravesical

instillation of Bacille Calmette-Guerin (BCG). This treatment is widely considered to be the gold standard for intermediate to high risk NMIBC due to its high response rate and capability to reduce the disease progression by activating the immune system of patients. However, BCG fails in about 20–40% of patients during the follow up. Furthermore, BCG treatment is associated with the risk of mycobacterial infection^{4–7}.

¹Institute for Bioengineering of Catalonia (IBEC), The Barcelona Institute of Science and Technology (BIST), Barcelona, Spain. ²PHI BIOMED Co., Seocho-gu, Seoul, Korea. ³Department of Urology, Seoul National University College of Medicine, Jongno-gu, Seoul, Korea. ⁴Department of Urology, Seoul National University Hospital, Jongno-gu, Seoul, Korea. ⁵CIC biomaGUNE, Basque Research and Technology Alliance (BRTA), San Sebastian, Guipúzcoa, Spain.

⁶Department of Materials Science and Engineering, Pohang University of Science and Technology (POSTECH), Pohang, Gyeongbuk, Korea. ⁷Graduate School of Medical Science and Engineering, Korea Advanced Institute of Science and Technology (KAIST), Yuseong-gu, Daejeon, Korea. ⁸Institució Catalana de Recerca i Estudis Avançats (ICREA), Passeig Lluís Companys 23, Barcelona, Spain. ⁹These authors contributed equally: Hyunsik Choi, Seung-hwan Jeong.

✉ e-mail: mdrafael@snu.ac.kr; gykoh@kaist.ac.kr; ssanchez@ibecbarcelona.eu; skhanb@postech.ac.kr

STimulator of INterferon Genes (STING) mediates innate and adaptive immune systems as a signaling molecule which resides in endoplasmic reticulum. Aberrant cytoplasmic exposure of double strand DNAs is recognized by cyclic GMP-AMP synthase to trigger STING pathway^{8,9}. In tumors, activated STING pathway recruits cytotoxic T cells to tumor site contributing to antitumor immunities^{10,11}. Recently, nanocarriers encapsulating natural ligands for STING, cyclic dinucleotides (CDNs), have shown outstanding antitumor efficacy in preclinical studies and several STING agonists have been investigated for human clinical trials^{12–15}. However, in the case of bladder cancer, STING agonist delivery with conventional nanocarriers is hard to achieve via intravesical injection, because urinary bladder is a hollow viscus filled with urine and urothelial cells are covered with a glycosaminoglycan (GAG) layer which hinders the penetration of therapeutics as well as toxins. Furthermore, the intravesically injected therapeutics can be easily cleared from the bladder because of the frequent urination. Accordingly, a special modality to deliver the STING agonist rapidly and efficiently into the bladder wall is highly required to meet these medical unmet needs.

Self-propelling micro/nanomotors (MNM)s have been considered as promising modalities for drug delivery due to their superiorities including navigation with tactic behavior, high biological barrier penetration and rapid drug transport with high drug delivery efficiency^{16–18}. Especially, utilizing enzymes as the engine of MNMs for self-propulsion is emerging with the use of endogenous fuels, enabling the on-site activation of nanomotors as a fully biocompatible robot^{19–21}. Moreover, the library of enzyme/substrate combination allows the design of application-tailored enzymatic nanomotors, such as urease-powered nanomotors in a bladder containing a high concentration of urea^{22–26}. Although a lot of enzyme-powered MNMs have been proposed, there are few reports on MNMs for the practical disease treatment.

Here, we develop a biodegradable urease-powered nanomotor containing STING agonist (STING@nanomotor) for bladder cancer immunotherapy (Fig. 1a). We choose the biopolymers of chitosan and heparin as a chassis of nanomotor, because these biopolymers have opposite charges for the effective encapsulation of negatively charged STING agonist during the formation of nanocomplex via electrostatic interaction. In addition, chitosan is a biodegradable natural cationic polysaccharide with good biocompatibility and muco-adhesiveness for binding and penetrating the mucus layer on the bladder wall²⁷. The urease-powered nanomotors show not only ballistic motion but also swarming behavior in the presence of urea (50–200 mM). After intravesical instillation, the nanomotors in the presence of urea evenly spread throughout the bladder to efficiently adhere and penetrate through the GAG layer. Even after several urination, a considerable amount of nanomotors remain in the bladder. We assess in vivo antitumor effect of STING@nanomotor and the recruitment of activated T cells for the treatment of NMIBC.

Results

Synthesis of urease-powered nanomotor containing STING agonist

STING@nanomotor was fabricated via 3 steps as schematically shown in Fig. 1b. First, chitosan and heparin were complexed by electrostatic crosslinking between positively charged amine groups of chitosan and negatively charged sulfate groups of heparin. Second, negatively charged STING agonist was encapsulated into the nanocomplex by electrostatic interaction under sonication. As shown in Supplementary Fig. 1a, the absorbance peak of free STING agonist was clearly observed at 252 nm wavelength due to the benzene group and the same peak around 252 nm was also detected in the group of STING@nanocomplex, indicating the successful loading of STING agonist in the nanocomplex. To optimize the loading of STING agonist, we assessed the loading efficiency of STING agonist according to the ratio of

components (chitosan: heparin: STING agonist) (Supplementary Fig. 1b). At the ratio of 2:0.5:0.2, the STING agonist was maximally loaded with a loading efficiency of 83.5%, as shown in the zeta potential analysis (Supplementary Fig. 1c). Under the optimal condition, we immobilized the urease onto the chitosan of nanocomplex with glutaraldehyde.

After that, we investigated the characteristic morphology and size of STING@nanomotor via transmission electron microscopy (TEM) and dynamic light scattering (DLS) (Supplementary Fig. 1d, e). STING@nanomotor showed a round shape with a size of *ca.* 600 nm. The hydrodynamic size of STING@nanomotor was slightly bigger than that of STING@nanocomplex due to the immobilization of urease onto the surface of STING@nanocomplex. The hydrodynamic size of STING@nanomotor was *ca.* 800 nm by DLS which was bigger than that of TEM, because chitosan and urease interacted dynamically with water molecules. In addition, zeta potential analysis showed that the surface charge of STING@nanocomplex (15 mV) was changed to −3.4 mV after immobilization of urease due to the negative charge of urease (Supplementary Fig. 1f). From the results, we could confirm the successful immobilization of urease onto the surface of STING@nanocomplex.

We compared the activity of immobilized urease and free urease with a urease activity assay kit (Supplementary Fig. 2a). First, we quantified the immobilized urease via Bradford assay and measured the urease activity with an equivalent amount of free urease. Remarkably, in consideration of ammonia generation for a unit time, the normalized activity of immobilized urease was 1.3-fold higher than that of free urease. This phenomenon might be ascribed by the improved stability and tolerance to pH and temperature of immobilized urease than free urease in aqueous environment^{28,29}. After that, we investigated in vitro release of STING agonist for 60 h in phosphate buffer at 37 °C (Supplementary Fig. 2b). In both conditions (pH 7.4 and 6), STING agonists were slowly released from the nanomotor, although the release profile in acidic condition (pH 6) showed more release of STING agonist than that of neutral (pH 7) for 60 h. This result might be ascribed to the partial swelling of chitosan in acidic condition, making nanomotors more susceptible to release STING agonist. In addition, we investigated in vitro stability of nanomotors by measuring the amount of released heparin from STING@nanomotors and the hydrodynamic size change of nanomotors with the incubation of lysozyme (Supplementary Fig. 2c, d). The STING@nanomotor appeared to be stable during the release period of STING agonist (Supplementary Fig. 2b, c). In contrast, the size of nanomotor was significantly decreased in the presence of lysozyme, reflecting the biodegradability of STING@nanomotor under in vivo environments with sufficient enzymes (Supplementary Fig. 2d).

In vitro dendritic cell activation

We evaluated the cellular uptake of STING@nanomotor using a murine dendritic cell line (JAWS II), because the uptake into cells is prerequisite for triggering STING pathway (Supplementary Fig. 3a). FITC labeled STING@nanomotor was incubated with dendritic cells for 2 h. STING@nanomotors were slightly internalized into dendritic cells after 1 h and the uptake was significantly increased after 2 h. Then, we investigated the mechanism for the dendritic cellular uptake of STING@nanomotors (Supplementary Fig. 3b). Since chitosan is known to be taken up into cells mostly via caveolin or clathrin mediated endocytosis, we blocked these receptors to compare the cellular uptake of STING@nanomotors. Without any blocking agents, STING@nanomotors were well internalized into dendritic cells. However, after blocking caveolin or clathrin receptors, the normalized green fluorescence was significantly reduced to 0.45 and 0.15, respectively (Supplementary Fig. 3c). Moreover, in both receptors blocking group, the green fluorescence could not be detected in dendritic cells, indicating that almost all of STING@nanomotors were

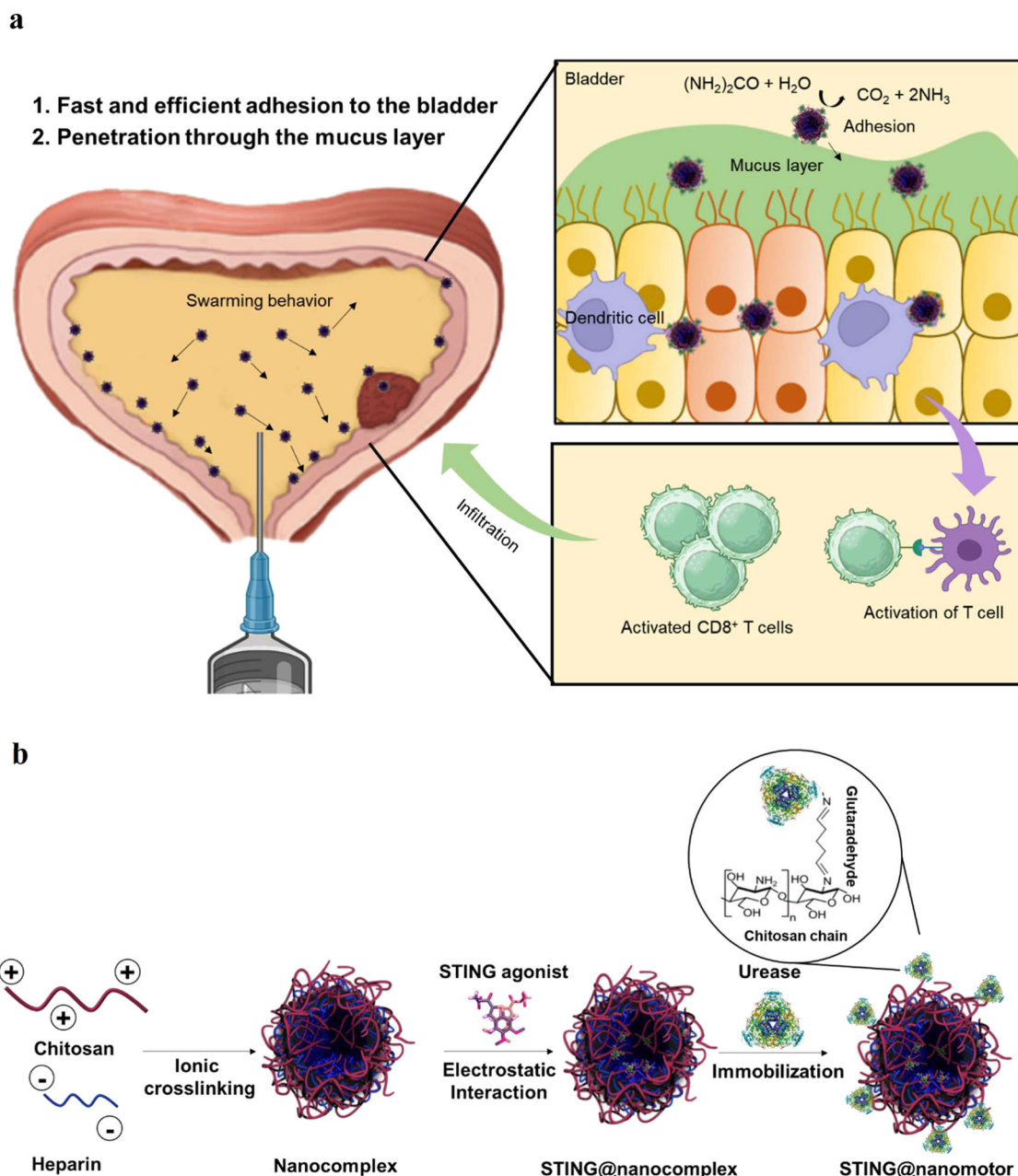


Fig. 1 | Schematic illustration of urease-powered nanomotor. a The intravesical delivery of urease-powered nanomotors for bladder cancer immunotherapy and **(b)** the preparation procedure of urease-powered nanomotors containing STING

agonist (STING@nanomotor, size = ca. 600 nm) by the electrostatic interaction of chitosan and heparin. **a** created in BioRender. Choi, H. (2024) <https://BioRender.com/ui3b061>.

internalized into dendritic cells via caveolin and clathrin mediated endocytosis^{30,31}.

After that, we investigated the uptake of STING@nanomotor into several types of cells (bladder cancer cell, endothelial cell) (Supplementary Fig. 4a). Like dendritic cells, the nanomotors could be taken into these cell lines efficiently. In addition, we investigated the effect of STING and STING@nanomotor on bladder cancer cells (Supplementary Fig. 4b). STING and STING@nanomotor showed negligible cytotoxicity on the bladder cancer cell, indicating that STING@nanomotor did not cause any cytotoxicity to bladder cancer cells directly. With confirming the cellular uptake, we investigated the STING pathway activation of dendritic cells (Supplementary Fig. 5a). After incubation of samples (nanomotor, free STING agonist and STING@nanomotor) for 24 h, we measured the expression of CD 80

and CD 86 on dendritic cells as dendritic cell activation markers via the immunofluorescence method. As expected, the empty nanomotor could not activate the dendritic cells with the negligible fluorescence of markers. Free STING agonist group showed weak fluorescence of CD 86 and CD 80 with the expression ratio of 21.5 and 18.6%, respectively (Supplementary Fig. 5b). Since STING agonist is an anionic and highly water-soluble molecule, this molecule does not readily cross the cellular plasma membrane to the cytosol where STING is located. In contrast, the fluorescence of CD 86 and CD 80 in STING@nanomotor group was noticeable with the expression ratio of 82.1 and 79.6%, respectively. On top of that, we examined *in vitro* secretion of cytokines and chemokines from dendritic cells after incubation with samples (control, nanomotor, free STING and STING@nanomotor) (Supplementary Fig. 6). In accordance with the enhanced uptake,

STING@nanomotor significantly increased the release of interferon (INF)- β , tumor necrosis factor (TNF)- α , and interleukin-6 (IL-6) in comparison with other groups.

Motion analysis of single nanomotor

The urease-powered nanomotor is propelling in the presence of urea by converting urea into ammonia and carbon dioxide as follows: $(\text{NH}_2)_2\text{CO} + \text{H}_2\text{O} \rightarrow \text{CO}_2 + 2\text{NH}_3$. According to our recent studies^{32,33}, molecularly unbalanced distribution of enzymes on the surface of nanomotors enabled the propulsion of synthetic motors via biocatalytic conversion. The motion profile of urease-powered nanomotors was analyzed in the presence of urea at the concentrations of 0, 50, 100 and 200 mM. We used an optical tracking method to obtain the tracked trajectories of nanomotors, which were recorded for 15 s with 40 frames per sec. The mean-squared displacement (MSD) was calculated from the trajectories (Supplementary Fig. 7a) and the velocity was obtained by fitting the MSDs (Supplementary Fig. 7b). Without urea, the nanomotors moved randomly by Brownian motion with the mild increase of MSD (Supplementary Fig. 7c and Supplementary Movie 1). However, when urea was added (50, 100 and 200 mM), the nanomotors moved fast with the steep increase of MSD curve (Supplementary Movie 2, 3 and 4). The increase of slope in the nonlinear MSD curve was observed just like a typical shape for ballistic motion, reflecting that the urease-powered nanomotor would be effectively propelled in the bladder.

Swarming behavior of nanomotors

The swarming behavior of nanomotors is very important, because the nanomotor can only perform the complicated tasks in the form of not an individual nanomotor but the swarm of nanomotors^{34–36}. A 5 μL droplet of nanomotors suspension was placed onto a Petri dish containing PBS or urea solution and swarming behaviors were recorded for 90 s (Supplementary Fig. 8 and Supplementary Movie 5–8). To investigate swarm dynamics, we then generated density maps. These were obtained by representing the pixel intensity values of video frames using a colormap (Fig. 2a and Supplementary Fig. 9) and projection intensity (Fig. 2b and Supplementary Fig. 10). The results suggested that after addition of the droplet in PBS, the nanomotors stayed at the seeding point following a stochastic distribution with small expansion area after 90 s. In contrast, in the urea solution, the swarms were expanding more efficiently and showed an increased expansion area with increasing urea concentration from 50 to 200 mM. In addition, we carried out particle image velocimetry (PIV) analysis on the optical microscopic videos (Fig. 2c and Supplementary Fig. 11) to assess how the swarms moved at specific time durations (10–12 s, 45–47 s, 80–82 s). PIV is an optical technique to visualize the fluid flow related to particle motility with fluid and particle displacements in the form of vector fields. PIV mapping showed that the higher velocity vectors were frequently observed at the higher concentration of swarms for all time duration. The expansion area for 90 s (Fig. 2d and Supplementary Movie 9–12) also showed that the swarms covered the area more efficiently at the higher concentration of urea, in consistent with density maps and PIV analysis. After 90 s, most of nanomotors without urea sank to the bottom of the aqueous solution with little expansion of swarm (Supplementary Fig. 12). However, in the presence of urea, the nanomotors could be observed at every height of solution with a large area in a Petri dish after 90 s, demonstrating that the swarm with urea expanded in 3-dimension (3D). Especially, the shape of expansion was gradually changing from round to ring shape and the shell thickness became thinner with increasing urea concentration (Fig. 2e). This phenomenon could be ascribed to the vortex-ring theory³⁷. When the droplet was discharged into a static fluid containing urea, the shear imposed at the interface between the two fluids slowed down the outer layer of the droplet relatively to the inner layer of fluid, rolling up in the form of vortex ring. The thickness of ring was

decreased with increasing fluid velocity. From the theory, a vortex ring can travel for relatively long distance, indicating that the swarms can effectively reach the bladder wall in 3D hollow structure of bladder in the presence of urea.

We further studied in vivo swarming behavior of nanomotors in a bladder after intravesical instillation, which is a common administration route to maximize the concentration of drugs in a bladder³⁸. We radiolabeled the nanomotor with ^{18}F to observe the phenomenon in a bladder using positron emission tomography-computed tomography (PET-CT) (Fig. 3a). PET-CT is a suitable imaging modality to study the swarming behavior of nanomotors, because PET-CT is a fully translational tool detecting gamma ray with no tissue penetration limit. In addition, it is extremely sensitive, providing good quality images by administering sub-pharmacological dosages of the radiolabeled entity^{39,40}. We removed the residual urine in a bladder to make the empty bladder before intravesical instillation for controlling the urea concentration precisely (0 and 200 mM). When ^{18}F -nanomotors without urea were intravesically injected, we observed a uniform distribution of the radioactivity immediately, but the phase of radioactivity was gradually separated for 45 min (left panel of Fig. 3b, Supplementary Movie 13). However, when administered with 200 mM urea, homogeneous distribution of nanomotors was observed for 45 min (right panel of Fig. 3b, Supplementary Movie 14). The 3D reconstructed images also showed that the nanomotors with urea distributed more evenly than that without urea in 3D bladder for 45 min (Fig. 3c, Supplementary Movie 15 and 16). These observations were further confirmed by analyzing the concentration of radioactivity in two volumes of interests (VOIs). Indeed, for ^{18}F -nanomotors injected in 200 mM urea, the time activity profile showed that the concentration of radioactivity in both regions was close to 50% for 45 min (Fig. 3d), demonstrating the homogeneous (mixing) concentration of radioactivity in the bladder. To the contrary, time activity curves under the control condition showed a gradually divergent trend (Fig. 3e), indicating that the concentration of radioactivity in the bladder was heterogeneous (two-phases). Since the swarms of ^{18}F -nanomotor with urea could actively move and enhance mixing in the bladder, phase separation was prevented. On top of that, because the chitosan based nanomotor is mucoadhesive, the wide spread of nanomotor throughout the bladder can significantly increase the probability of adhesion to the GAG layer and penetrate through the layer without clearance by urination.

Penetration and retention of nanomotors in the bladder

We prepared two groups for STING@nanocomplex (passive particle without urease) and STING@nanomotor to evaluate the penetration and retention of nanomotors. We labeled the nanocomplex and the nanomotor with a fluorescence dye and measured the fluorescence intensity in the bladder after intravesical instillation by Z-stack imaging of flattened bladder tissues, fluorescence imaging of sectioned bladder and IVIS imaging in the whole bladder (Fig. 4a). First, we measured the fluorescence of bladder for 120 min after instillation of samples (Fig. 4b–d). The bladders were excised from the mice and opened to flatten for measuring the fluorescence by depth. After 30 min, the fluorescence of nanocomplex could not be observed in ex vivo bladder wall. In contrast, the bladder after nanomotor injection showed noticeable fluorescence, reflecting that the propulsion of nanomotors could efficiently attach to the mucus layer and penetrate the bladder wall. After 120 min, the fluorescence of nanomotors was observed much stronger than that of nanocomplex. Second, we measured the fluorescence of sectioned bladder tissue after 12 h-post instillation to confirm the penetration and retention of samples in the bladder even after several urination for 12 h (Fig. 4e). As shown in the bladder section after 12 h, nanomotors distributed broadly in the bladder wall and the considerable amount of nanomotors were retained in bladder, whereas nanocomplex was much less retained in the bladder wall.

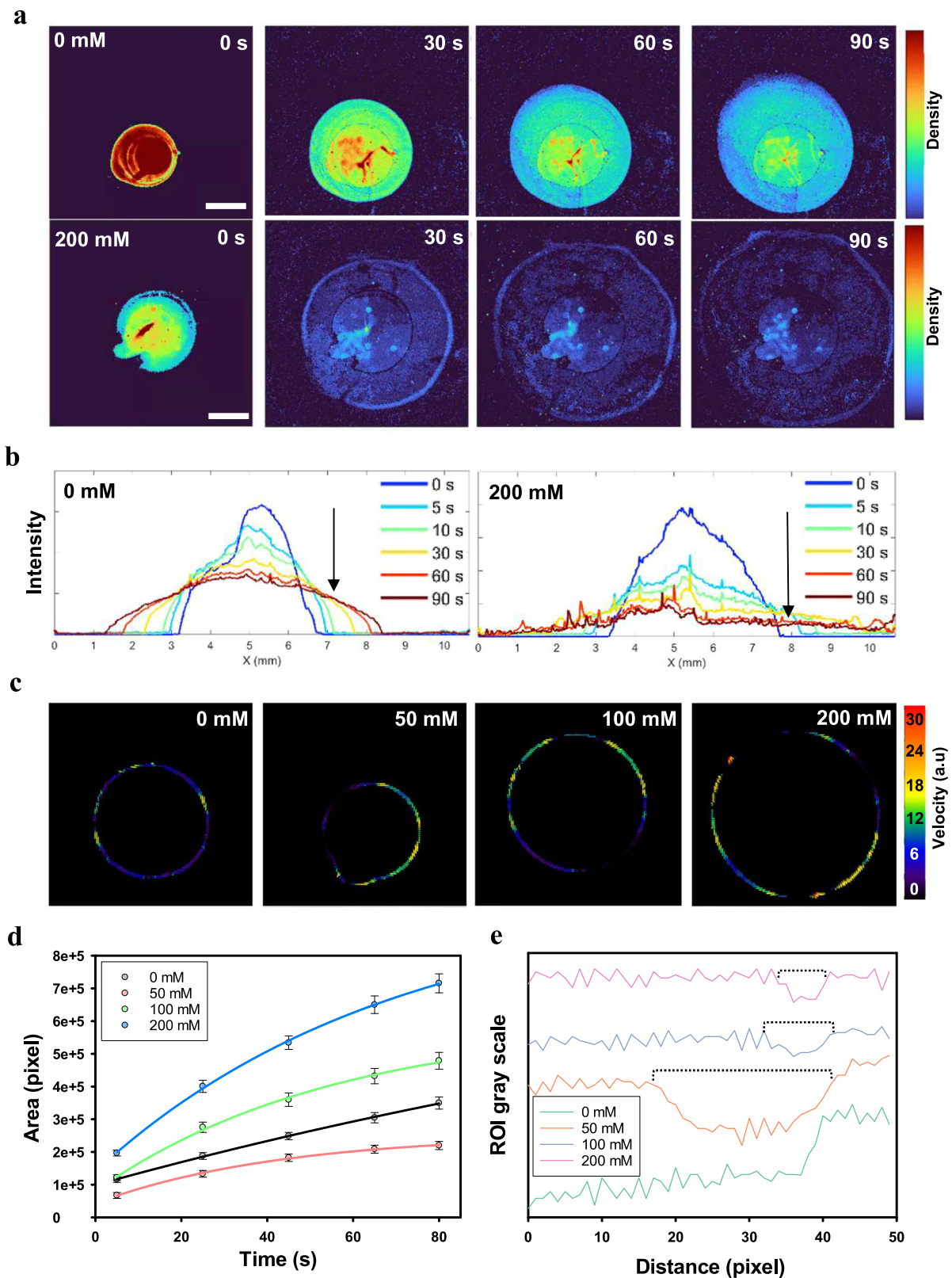


Fig. 2 | In vitro motion analysis of nanomotors. a Density maps of swarming in the presence (upper panel) and in the absence of urea (lower panel) for 90 s (scale bar = 2 mm) and (b) the corresponding X axis projection with time (0, 5, 10, 30, 60, and 90 s). **c** Particle image velocity (PIV) analysis of swarm according to the urea concentration for 2 s (45 s–47 s). The density maps and PIV images are representative of 3 independent experiments. **d** Expanding area according to the urea

concentration for 90 s. Data are presented as mean values and error bars represent the S.D. ($n = 3$ per group, biological replicates). **e** The gray scale of ROI region indicated in supplementary Fig. 4c at 30 s. The gray scale of ROI region is representative of 3 independent experiments. Black dot lines indicate the width of ring pattern in swarm. Source data are provided as a Source Data file.

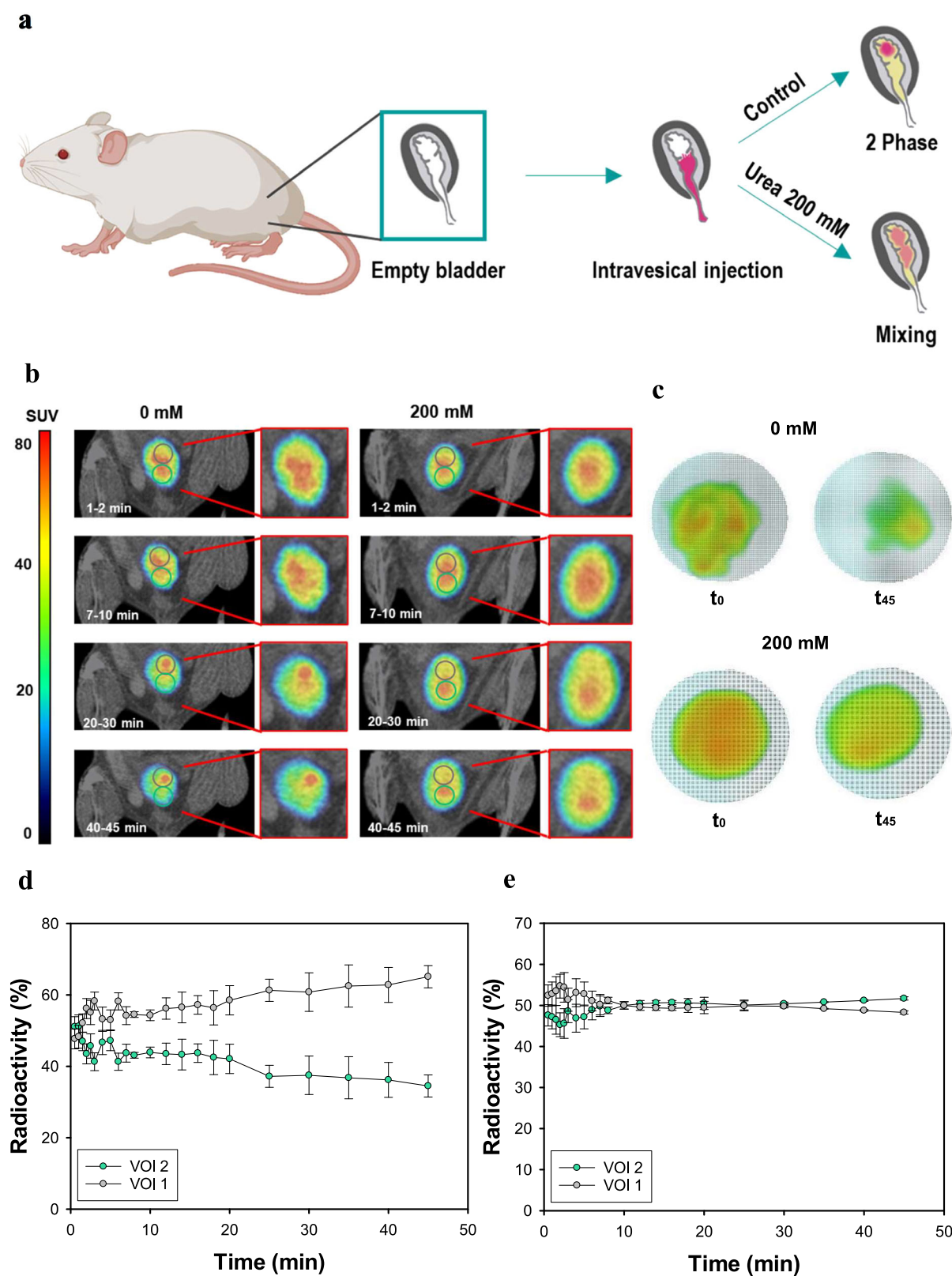


Fig. 3 | PET-CT analysis of ^{18}F -nanomotors after intravesical instillation.

a Schematic illustration for the administration to analyze in vivo swarming behavior of nanomotors. **b** PET-CT images for 45 min after the intravesical instillation of ^{18}F -nanomotors in the presence and in the absence of 200 mM urea, and **(c)** the corresponding 3D reconstructed images at 0 and 45 min. The

PET-CT images are representative of 3 independent experiments. Quantitative analysis of the VOIs **(d)** without and **(e)** with urea for 45 min. Data are presented as mean values and error bars represent the S.D. ($n = 3$ mice per group). Source data are provided as a Source Data file. **a** created in BioRender. Choi, H. (2024) <https://BioRender.com/u13b061>.

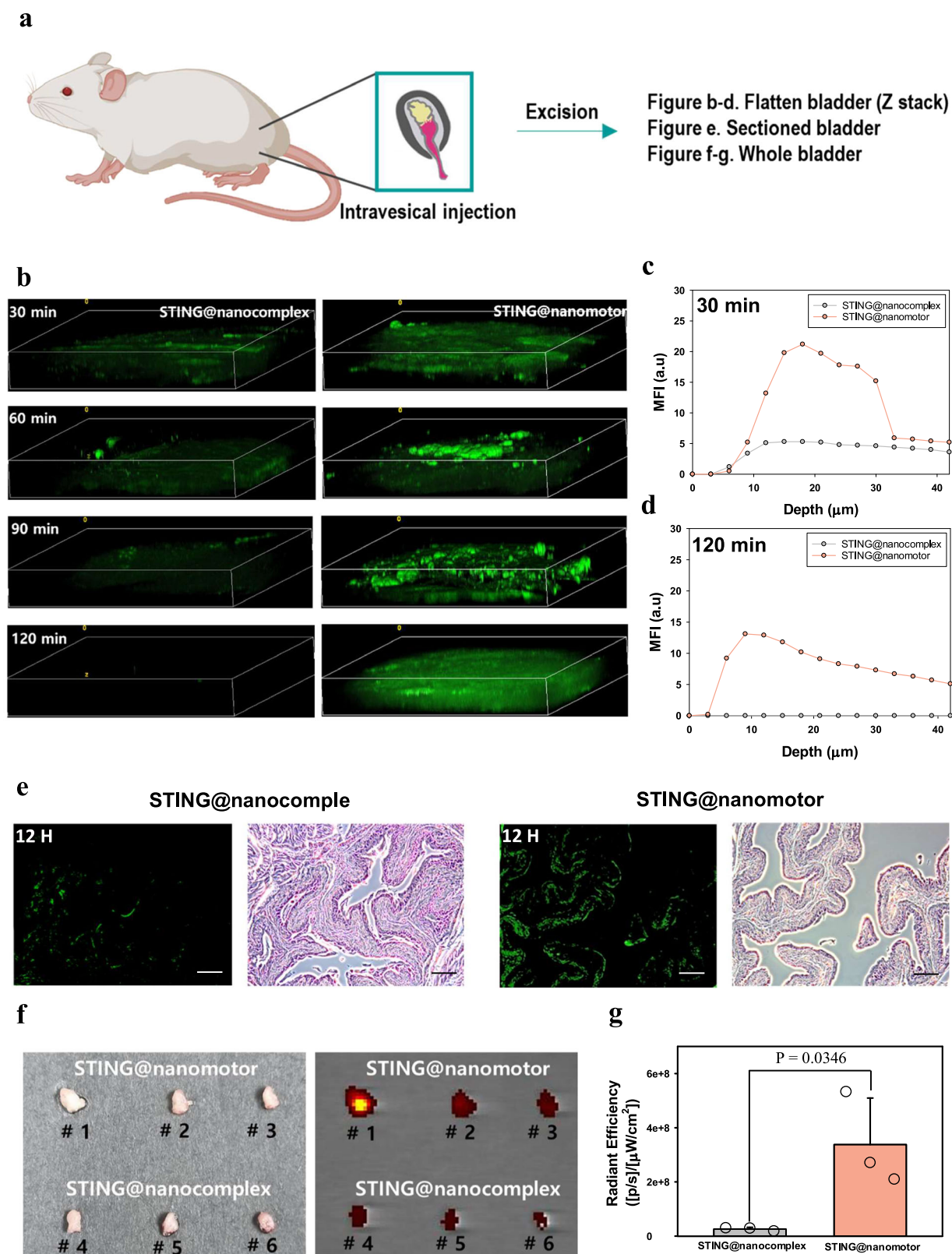


Fig. 4 | In vivo penetration and retention of STING@nanomotor after intravesical instillation. **a** Schematic illustration for the penetration and retention tests of nanomotors after intravesical instillation by using 3 different ways. **b** 3D fluorescence images after injecting fluorescence dye labeled STING@nanomotors and STING@nanocomplex in the bladder for 120 min and the corresponding mean fluorescence intensity (MFI) at **(c)** 30 min and **(d)** 120 min. **e** Bladder section after 12 h post-intravesical injection of STING@nanomotors and STING@nanocomplex

in mice (scale bar = 100 μm). The fluorescence images and corresponding MFI are representative of 3 independent experiments. **f** Photograph (left) and IVIS imaging (right) of bladders after 12 h post-intravesical injection of samples and **(g)** the corresponding total radiant efficiency of bladders. Data are presented as mean values and error bars represent the S.D., and statistical analysis was performed via two-sided t-test ($n = 3$ mice per group). Source data are provided as a Source Data file. **a** created in BioRender. Choi, H. (2024) <https://BioRender.com/u13b061>.

Finally, we investigated the retention of nanomotors with the whole bladder via IVIS imaging (Fig. 4f, g). The nanomotor injected bladders (#1, #2 and #3) showed stronger fluorescence than nanocomplex injected bladders (#4, #5 and #6), in consistent with the fluorescence imaging of sectioned bladder. In addition, we measured the fluorescence intensity of STING agonist from the extracted urine to further confirm the clearance (Supplementary Fig. 13). Above 80% of injected STING was removed very fast from the bladder within 4 h, whereas STING@nanomotor could be detected in the urine for 12 h, exhibiting the prolonged retention of STING@nanomotor in the bladder, in consistent with IVIS imaging (Fig. 4f, g). Before conducting in vivo experiments with mice, we investigated in vivo blood biochemistry and histological analysis to confirm the biosafety in vivo (Supplementary Fig. 14). There was no lesion or inflammation in the bladder section after treatment of STING@nanomotor. In addition, there was no significant difference of parameters including MCV, RDW, HCT, HGB, MCH, MCHC, CREA and BUN in the blood after treating with STING@nanomotor.

Antitumor effect of nanomotor on bladder cancer

To investigate the antitumor effect of STING@nanomotor on bladder cancer, we prepared bladder cancer model animals by intravesical injection of MB49 bladder cancer cells. After 4 and 8 d of tumor cell instillation, each sample was intravesically injected including PBS as a control, nanomotor as a vehicle, STING, STING@nanocomplex and STING@nanomotor (Fig. 5a). STING activation by free STING agonist or STING@nanocomplex reduced the bladder tumor growth by 28.5% and 38.0%, respectively. Notably, STING@nanomotor strongly and significantly inhibited tumor growth by 94.2% compared with the control (upper panel of Fig. 5b, c). We monitored the tumor growth by bioluminescence imaging in a murine bladder cancer model using MB49-luc2 cells transfected with firefly luciferase gene *luc2* (Supplementary Fig. 15). The luciferase intensity was well matched with the thickness of sectioned bladder. Especially, at 14 d, the luciferase intensity was very low in the group of STING@nanomotor, indicating the strong inhibition effect on bladder tumor growth.

We evaluated CD8 T cell infiltration and expressions of cascading cytokines of STING pathway to study the mechanism of the treatment. When we compared intratumoral CD8 T cell infiltration, STING@nanomotor showed significant CD8 T cell infiltration by 11.2-fold compared with the control of PBS, which elucidated the powerful antitumor effect by STING@nanomotor (lower panel of Fig. 5b, c). The results confirmed that STING@nanomotor efficiently activated the dendritic cells in the bladder wall to recruit CD8 T cell in bladder. In addition, the expressions of cascading cytokines of STING pathway including interleukin (IL)-1 β , IL-6, IFN- β , and C-X-C motif chemokine ligand (CXCL) - 10 were assessed on 8 d after tumor cell instillation (Fig. 5d). After 24 h of intravesical treatment, IL-6, IFN- β , and CXCL-10 were elevated by STING@nanomotor as high as 2.43, 6.58, and 2.55-fold compared with the control, respectively (Fig. 5e), demonstrating the highly activated STING pathway by STING@nanomotor.

After confirming the enhanced tumor growth inhibition of STING@nanomotor, we further investigated the antitumor and pro-tumor immune responses of STING@nanomotor by the flow cytometry. First, we assessed the phenotype of T cells in the bladder including CD8⁺ T cells and CD4⁺ T cells (Fig. 6a, c). The STING and STING@nanomotor treatments increased CD8⁺ T cell infiltration, whereas CD4⁺ T cell infiltration was not changed significantly. This infiltration was more pronounced with STING@nanomotor treatment compared with that of STING. We also analyzed the regulatory T cells (T_{reg} cells) in the bladder, since T_{reg} cells inhibit the antitumor effects of cytotoxic T cells (Fig. 6b, c). The intravesical treatment with STING@nanomotor significantly reduced T_{reg} cell populations (0.63% of whole single cells) in the bladder compared to the control group (2.45% of whole single cells). From the analysis of T cell population, we

found that STING@nanomotor significantly enhanced cytotoxic CD8⁺ T cell and reduced T_{reg} cell in the bladder for cancer immunotherapy.

Tumor-associated macrophages (TAMs) also orchestrate the antitumor immunity. For examples, M1 polarized macrophages have antitumoral effects, and M2 polarized macrophages have protumoral effects and suppress the cytotoxic T cell activity on tumor cells. While STING activation is known to enhance cytotoxic T cell activity and infiltration, its effect on tumor-associated macrophages is less clear⁴¹. As shown in Supplementary Fig. 16, STING@nanomotor showed the increased population of TAM. Meanwhile, STING and STING@nanomotor did not significantly affect the polarization of tumor-associated macrophages in accordance with the recent reports^{42,43}. In addition, we evaluated in vivo dendritic cell maturation by the flow cytometry analysis of CD80, CD86, and MHC-II expression profiles on dendritic cells (Fig. 6d, e). Remarkably, the STING activation with STING@nanomotor enhanced the dendritic cell maturation, showing a significant increase of CD 80 (*ca.* 3-fold increase of MFI), CD 86 (*ca.* 2.3-fold increase of MFI) and MHC-II (*ca.* 3.5-fold increase of MFI) compared to the control group.

Comparison with BCG treatment and anti-PD1 therapy

The intravesical BCG treatment is the gold standard for intermediate or high-risk non-muscle invasive bladder cancers. To support the clinical feasibility, we compared the antitumor effect of STING@nanomotor with BCG therapy (Fig. 7a). Remarkably, BCG did not significantly suppress tumor growth in a murine bladder cancer model using MB49 cells. In contrast, STING@nanomotor suppressed tumor growth more dramatically than BCG treatment. On top of that, we investigated the synergistic effect of combining the nanomotor with immune checkpoint inhibitors (ICIs) in the in vivo setting (Fig. 7b). Pembrolizumab, an anti-PD-1 inhibitor, rescues exhausted T cells and activates them to target tumor cells, drastically enhancing anti-tumor immunity^{44–46}. Pembrolizumab is already clinically available for the treatment of bladder cancer. It is indicated for non-muscle invasive bladder cancers, including carcinoma in situ lesions. The antitumor effect of an anti-PD-1 antibody and its combinatory effect with STING@nanomotor were assessed in the murine bladder cancer model. Although the anti-PD-1 antibody slightly inhibited bladder tumor growth, it was less effective than STING@nanomotor monotherapy. Surprisingly, the combination therapy of anti-PD-1 antibody and STING@nanomotor almost completely eradicated the bladder tumor growth. From the results, we could confirm the superior tumor growth inhibition efficacy of nanomotors to the clinical gold standard BCG treatment, and the synergistic effect of the nanomotor and the conventional anti-PD-1 antibody, demonstrating the feasibility of STING@nanomotor as a next-generation therapeutic system for the treatment of bladder cancers.

Discussion

Enzyme powered nanomotors have been extensively investigated to demonstrate the proof-of-concept for active and targeted drug delivery applications^{20–26}. Among various therapeutic applications, it seems clinically feasible to apply nanomotors especially for the treatment of bladder diseases and stomach diseases^{22–24}. However, it is still challenging to show the better therapeutic efficacy of nanomotor systems than that of conventional therapeutic systems for the practical treatments of bladder diseases such as interstitial cystitis, overactive bladder, bladder cancer, and bladder prolapse. In this work, we successfully demonstrate the clinical feasibility of urease powered nanomotors containing STING agonist for bladder cancer immunotherapy with swarming analysis by in vitro simulation and in vivo PET-CT imaging. As reported elsewhere⁴⁷, cancer immunotherapy is greatly advantageous for preventing tumor metastasis and recurrence with its ability to build a strong immune memory in the body. Here, we report bladder cancer immunotherapy using urease powered nanomotors,

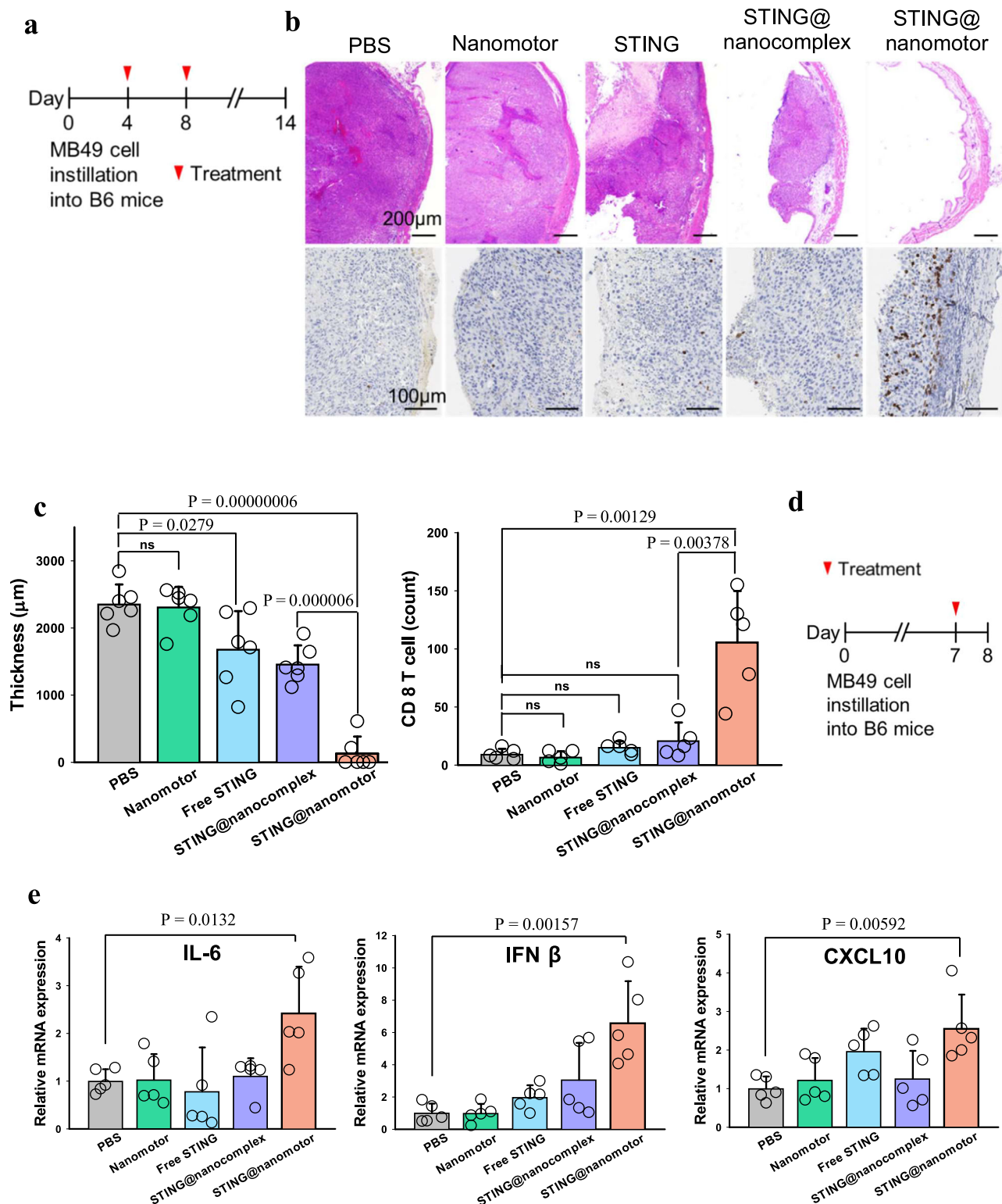


Fig. 5 | STING@nanomotor to inhibit bladder cancer growth by inducing antitumor immunity. **a** Diagram depicting the generation of MB49 bladder cancer in B6 mice and the treatment schedule. **b** Representative images for the comparison of tumor growth by H&E staining of bladder cancers (upper panel) and the CD8 T cell infiltration (lower panel) after each treatment. The H&E staining images are representative of 6 independent experiments and CD8 T cell immunohistochemical images are representative of 5 independent experiments. **c** Quantitative analysis for the tumor thickness and the CD8 T cell infiltration. Data are presented as mean

values and error bars represent the S.D. and statistical analysis was performed via two-sided t-test ($n = 6$ mice per group). **d** Diagram depicting the generation of MB49 bladder cancer and the treatment schedule to measure mRNA expression in the bladder. **e** mRNA expression of indicated genes following each treatment. Data are presented as mean values and error bars represent the S.D., and statistical analysis was performed via two-sided t-test ($n = 5$ mice per group). Source data are provided as a Source Data file.

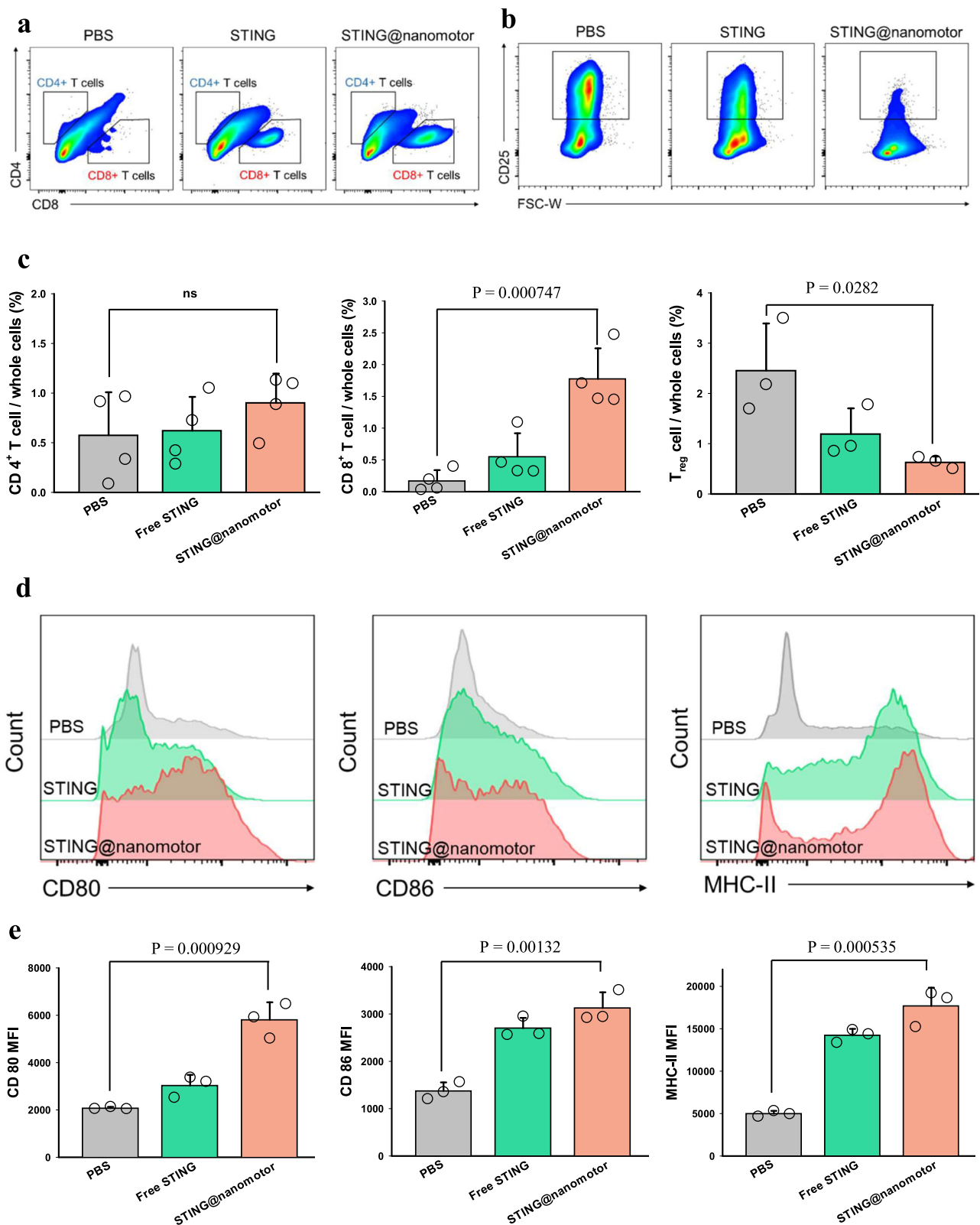


Fig. 6 | Immune response and pro-tumor response of STING@nanomotor. The representative flow cytometry plots of (a) CD4⁺ and CD8⁺ T cells, and (b) regulatory T cells. c The corresponding percentage of CD4⁺, CD8⁺ T cells ($n = 4$ mice per group) and regulatory T cells in whole bladder cells. Data are presented as mean values and error bars represent the S.D. and statistical analysis was performed via two-sided t-test ($n = 3$ mice per group). d The flow cytometry comparison of CD80, CD86, and MHC-II expression on dendritic cells from each bladder tumor and (e)

the corresponding mean fluorescent intensity of expressed CD80, CD86, and MHC-II. CD8⁺ T cells were identified as DAPI/CD45⁺/CD3e⁺/CD4⁺/CD8a⁺ cells, CD4⁺ T cells as DAPI/CD45⁺/CD3e⁺/CD8a⁺/CD4⁺ cells, T_{reg} cells as FVS450⁺/CD45⁺/CD4⁺/CD25⁺ cells and dendritic cells as DAPI/CD45⁺/CD11c⁺ cells. Data are presented as mean values and error bars represent the S.D., and statistical analysis was performed via two-sided t-test ($n = 3$ mice per group). Source data are provided as a Source Data file.

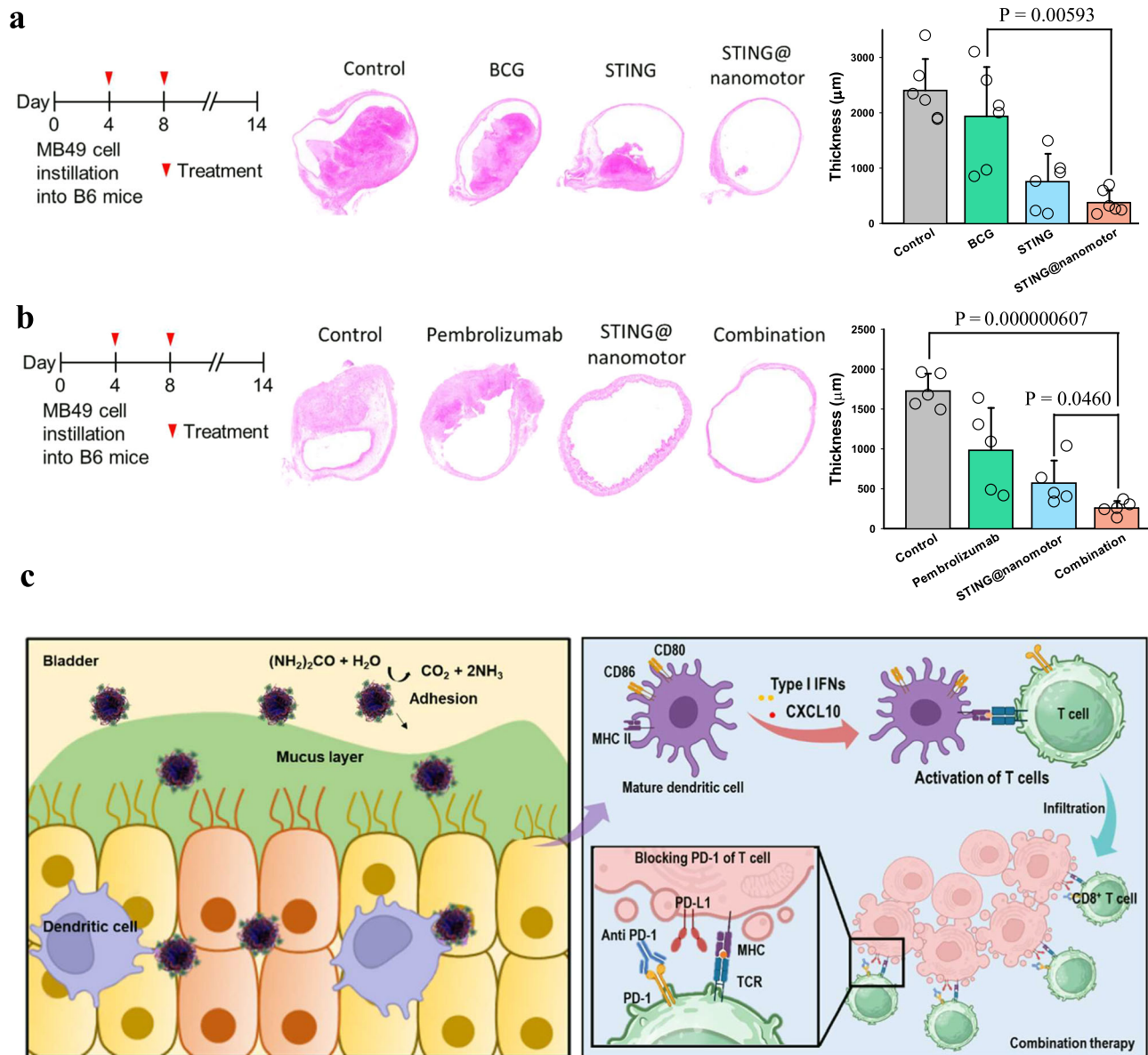


Fig. 7 | The anti-tumor effect of BCG treatment and anti-PD-L1 combination therapy with nanomotors. a The treatment schedule and the representative images of sectioned urinary bladder from the bladder cancer model prepared by using MB49 cells after each treatment (control, BCG, STING and STING@nanomotor) (left) and the corresponding thickness of bladder wall. Data are presented as mean values and error bars represent the S.D. and statistical analysis was performed via two-sided t-test ($n = 6$ mice per group). **b** The treatment schedule and the representative images of sectioned urinary bladder from the bladder cancer

model after each treatment (control, anti-PD-1, STING@nanomotor and combination) (left) and the corresponding thickness of bladder wall. Data are presented as mean values and error bars represent the S.D. and statistical analysis was performed via two-sided t-test ($n = 5$ mice per group). **c** Schematic illustration for the overall mechanism of anti-PD-L1 combination therapy with STING@nanomotor for bladder cancer immunotherapy. Source data are provided as a Source Data file. **c** created in BioRender. Choi, H. (2024) <https://BioRender.com/u13b061>.

showing the better anti-tumor effect of STING@nanomotor than those of the gold standard BCG therapy and an anti-PD-1 inhibitor of Pembrolizumab therapy in a murine bladder cancer model.

In our previous reports^{22–25}, we used 300 mM of urea for the propulsion of inorganic particle based nanomotors as an optimal concentration, which is a slightly high concentration in the real bladder. Since the chitosan/heparin nanocomplex (organic particle) is lighter than the inorganic particle such as silica particles and iron oxide particles, the lower concentration of urea could be used for the propulsion of STING@nanomotor, efficiently working in the real bladder. In addition, muco-adhesive chitosan is greatly advantageous for binding and penetrating the mucus layer on bladder wall²⁷. The biocompatible polymeric nanomotor system would be more feasible for

in vivo swarming behavior in the bladder and the practical treatment of bladder cancer with its reliable biosafety, biodegradability, low toxicity and high penetration and prolonged retention in the bladder. Furthermore, STING@nanomotor showed negligible cytotoxicity on the bladder cancer cell (Fig. S4b), indicating that STING@nanomotor did not kill the bladder cancer directly, but caused the immune responses for the bladder cancer immunotherapy. By combining the propulsion effect and superior properties of STING@nanomotor, we made several important big steps toward the futuristic translational medicine.

BCG is the attenuated strain of *Mycobacterium bovis*, which has been used as a vaccine against tuberculosis. The precise mechanism of BCG in bladder cancer treatment is not fully understood, but it has been presumed that the activation of immune response plays a key

role to activate antitumor immunities^{4–7}. Because of its in-born nature of BCG, it has several side effects such as hypersensitivity and infections resulting in severe complications. The intravesical instillation of BCG was adopted more than 40 years ago. The complete response rate of BCG therapy ranges from 50–70% after induction dose in the bladder cancer stage of Ta, T1, and T1c. However, it has been known that BCG fails in about 20–40% of patients during the follow up⁴⁸. In this work, we confirmed that the anti-tumor effect of nanomotors containing STING agonist was much better than that of BCG treatment, the gold standard therapeutic treatment in bladder cancers. In combination with the immune checkpoint inhibitor of anti-PD-1 inhibitor, STING@nanomotor achieved even greater anti-tumor therapeutic efficacy. As shown in Fig. 7c, intravesically injected STING@nanomotor efficiently penetrated through the mucus layer by self-propulsion and activated the dendritic cells to recruit activated T cells into the bladder tumor site. By blocking PD-1 expressed on the T cells with the anti-PD-1 inhibitor, CD8⁺ T cell was able to kill the bladder cancer cells significantly, confirming the feasibility as a next generation therapeutics for bladder cancer immunotherapy.

In conclusion, we developed a urease-powered nanomotor to actively deliver STING agonist for bladder cancer immunotherapy. The nanomotors were fully characterized by TEM, DLS analysis, UV-vis spectrometry, and urease activity tests. We assessed in vitro activation of dendritic cells with in vitro and in vivo swarming behavior analysis of nanomotors in the range of urea concentration in bladder (0–200 mM). After intravesical instillation, we corroborated the effective penetration and retention of nanomotors in bladder of mice. In bladder cancer bearing model mice, we successfully demonstrated the anti-tumor effect of nanomotors containing STING agonist (94.2% of inhibition after 14 d), recruitment of CD8⁺ T cells (11.2-fold compared with PBS) and the enhanced anti-tumoral immune response. Taken together, we could confirm the feasibility of urease-powered nanomotors as a promising treatment strategy for the bladder cancer immunotherapy.

Methods

Animals were maintained and handled in accordance with European Council Directive 2010/63/UE and Animal Care Committee of Seoul National University Hospital. All experimental procedures were approved by the CIC biomaGUNE ethics committee and local authorities (Diputación Foral de Guipuzcoa, PRO-AE-SS-276). All mice were fed with ad libitum access standard diet (PMI lab diet) and water and anesthetized by intraperitoneal injection of a combination of anesthetics (80 mg/kg of ketamine and 12 mg/kg of xylazine) before procedures and being euthanized.

Materials

Chitosan (low molecular weight), heparin sodium salt (from porcine intestinal mucosa), urease (from *Canavalia ensiformis*, type IX, powder, 50,000–100,000 units per gram of solid), glutaraldehyde solution (25%), urease activity assay kit, collagenase type2-II, formaldehyde, penicillin, streptomycin, dimethyl sulfoxide (DMSO), chlorpromazine, acetone, trifluoroacetic acid (TFA), methanol, dichloromethane, tert-butanol methyl benzoate, xylene, formaldehyde solution, hydrochloric acid (HCl), and genistein were purchased from Sigma Aldrich (St. Louis, MO). Fluorescein isothiocyanate (FITC)-heparin was purchased from Creative PEG works (Durham, NC). STING agonist (ADU-s100, STING) was purchased from Medchem express (Monmouth Junction, NJ). Allophycocyanine (APC)-anti mouse CD 86 and FITC-anti human CD 80, Bradford protein assay kit, Phosphate buffered saline (PBS), Dulbecco's modified Eagle medium (DMEM), alpha-modified medium (α -MEM), and fetal bovine serum (FBS), dispase were purchased from Thermo Fisher Scientific (Waltham, MA). Anti-CD8 antibody (Cat. 550281), Brilliant Blue 515 anti-mouse CD45 (Cat. 564590), RealYellow 586 anti-mouse CD11c (Cat. 753112), Brilliant Ultraviolet 737

anti-mouse CD80 (Cat. 612773), Brilliant Ultraviolet 737 anti-mouse CD45 (Cat. 748371), RealYellow 586 anti-mouse CD8a (Cat. 568163), RealYellow 586 anti-mouse CD4 (Cat. 568161), RealYellow 586 anti-mouse CD11b (Cat. 568485), Brilliant Ultraviolet 737 anti-mouse F4/80 (Cat. 749283) were purchased from BD bioscience (Franklin Lakes, NJ). Murine granulocyte-macrophage colony-stimulating factor (GM-CSF) was purchased from Peprotech (Cranbury, NJ). MB49 cell, HUVEC cell and JAWS II cell were obtained from ATCC (Manassas, VA). Brilliant Violet 421 anti-mouse CD86 (Cat. 105032), Alexa Fluor 647 MHC-II (Cat. 141712), Brilliant Violet 605 anti-mouse CD11c (Cat. 117334), Brilliant Violet 510 anti-mouse CD3 epsilon (Cat. 100353) were purchased from BioLegend (San Diego, CA). Anti-PD-1 antibody (Cat. BE0273) was purchased from InVivoMAb (Lebanon, NH). BCG (OncoTICE, Strain TICE) was purchased from Merk (Rahway NJ). D-luciferin was purchased from Promega (Madison, WI). DNase I was purchased from Roche (Basel, Swiss). Alexa Fluor 647 anti-mouse MHC-II (Cat. NBP2-21789AF647) was purchased from Novus Biologicals (Minneapolis, MN). CF488A anti-mouse CD4 (Cat. BNC882009-500) was purchased from Biotium (Fremont, CA). StarBright UltraViolet 400 anti-mouse CD25 (Cat. MCA1260SBUV400) was purchased from Bio-rad (Hercules, CA).

Synthesis of STING agonist encapsulating chitosan-heparin nanocomplex

First, chitosan-heparin nanocomplex was synthesized as previously reported elsewhere^{49,50}. In brief, 0.4, 0.5, or 0.6 mL of heparin (1 mg/mL) was added dropwise in 2 mL of chitosan solution (1 mg/mL in 1% acetic acid) to form chitosan-heparin nanocomplex. After that, 0.1 or 0.2 mL of STING agonist solution (2 mg/mL) was added to the resulting solution under sonication. To remove excess STING agonist, the solution was dialyzed against DI water for 3 days.

Synthesis of urease-powered nanomotor encapsulating STING agonist

Amine group of urease was conjugated with amine group of chitosan with a glutaraldehyde linker. One mL of urease solution (2 mg/mL in PBS) was added to 3 mL of glutaraldehyde solution (2.5%) and un-reacted glutaraldehyde was removed by dialysis against excess deionized (DI) water. After that, 1 mL of activated urease was added to 0.4 mL of as-prepared STING@nanocomplex solution for 1 h with constant stirring. After that, the urease functionalized STING@nanomotor solution was washed with PBS thrice by centrifugation (2000 g for 5 min) and dispersion with sonication for 3 min.

Characterization of urease-powered nanomotor encapsulating STING agonist

The size and morphology of STING@nanomotors were analyzed by transmission electron microscopy (TEM, H-7650, Hitachi, Tokyo, Japan) at 80 kV. Ten μ L sample of STING@nanomotor dispersed in aqueous solution (5 mg/mL) was deposited onto a copper grid. The grid was dried in air at room temperature for 3 days and then observed by TEM. In addition, the hydrodynamic diameters and zeta potential of the samples were measured by dynamic light scattering (DLS, Zetasizer Nano-ZS, Malvern, UK) at room temperature.

Quantification of urease on the nanomotor

The concentration of urease immobilized on the nanomotor was measured with the Bradford protein assay kit from Thermo Fisher Scientific according to the manufacturer's instruction.

Urease activity assay

The enzymatic activity of urease immobilized to the nanocomplex was measured with a commercial kit to determine the concentration of ammonia generated by the Berthelot's method. Using the nanomotors

at a concentration of 0.5 mg/mL, the experiment was performed according to the manufacturer's instruction.

In vitro cellular assessment of nanomotors

Murine dendritic cells (JAWS II) were cultured in an α -MEM containing 2 vol% FBS with ribonucleosides, deoxyribonucleosides, 4 mM L-glutamine, 1 mM sodium pyruvate, and 5 ng/mL murine GM-CSF at 37 °C in a humidified incubator under 5% atmospheric CO₂. As we previously reported elsewhere⁵¹, JAWS II cells were pre-treated with 10 μ g/mL of chlorpromazine and 70 μ g/mL of genistein to block the clathrin and caveolin mediated endocytosis. After that, FITC labeled nanomotors were incubated with pre-treated JAWS II cells for cell uptake test for 2 h. In addition, FITC labeled nanomotors were incubated with HUVEC and MB-49 cells for cellular uptake test for 2 h. Fluorescence images of cells were acquired by confocal microscopy (FV1000, Olympus, Japan). For STING activation test in dendritic cells, JAWS II cells were incubated with samples (PBS, STING, nanomotor and STING@nanomotor) for 12 h. For ELISA assay, after 12 h of incubation, supernatants were collected and stored at -80 °C until analyses for cytokines and chemokines detection. For fluorescence measurement, APC-anti mouse CD 86 (1:200 dilution) and FITC-anti human CD 80 (1:200 dilution) were treated with JAWS II cells, followed by PBS washing to remove unbound antibodies. Fluorescence images of cells were acquired by confocal microscopy and the expression ratio of CD 86 and CD 80 were evaluated by counting cells with fluorescence. MB-49 was cultured in serum-free medium supplemented with 10% FBS, 50 IU/mL penicillin, and 50 mg/mL streptomycin at 37 °C in a humidified incubator containing 5% atmospheric CO₂. In order to assess the cell viability with MTT solution, MB-49 cell was incubated with STING and STING@nanomotor for 24 h. Optical absorbance was measured with an ELISA microplate reader (Versamax, Molecular Devices, San Jose, CA).

Nanomotor movement analysis

An inverted microscope was used to observe and record the movement of nanomotors. The nanomotor sample solutions in simulated urine were placed on a glass slide and mixed well with simulated urine at the urea concentration of 0, 50, 100, and 200 mM. The movement of nanomotors in the urine was recorded for 15 s at a frame rate of 40 fps in a bright field. At least 20 nanomotors were analyzed per a condition, and the tracking path and the mean-squared displacement (MSD) were automatically analyzed with the Python software. After that, the survival was determined by fitting the MSD data to the following equation: $MSD(\Delta t) = (V \times \Delta t)^2 + 4 \times D_e \times \Delta t$.

Swarming behavior of nanomotor

The swarming behavior of nanomotors was assessed with a Leica DMI8 microscope, coupled with a Hamamatsu high-sensitivity CCD camera and a 2.5X objective. For that purpose, a petri dish was filled with 2 mL of either PBS or a urea solution in PBS (50, 100, and 200 mM) and placed in the microscope. A drop of 5 μ L of the nanomotors was then added carefully to the Petri dish and 90 s videos were acquired at a frame rate of 25 fps. The density maps of the optical videos were obtained by using a custom-made MATLAB code. Briefly, projection intensity was measured by summing up the intensity along X and Y. Expansion area was measured by converting gray scale images into binary images and subsequent summing up all pixels with intensity values above a certain threshold. The particle image velocimetry (PIV) analysis of optical videos was performed by using ImageJ. Prior to loading the images in the code, the frames of videos were treated to convert binary images. Then, cross-correlation analysis was performed with 64 interrogation window sizes.

Synthesis of [¹⁸F]F-PyTFP

[¹⁸F]F-PyTFP was synthesized in a Neptis® xSeedTM module (optimized radiochemical applications, ORA), following the previously reported method²⁵. In brief, [¹⁸F]Fluorine (produced by proton irradiation of an ¹⁸O-enriched water target) was trapped in an ion-exchange resin (Sep-Pak Accell Plus QMA Light) and subsequently eluted into a reactor vessel in a solution of Kryptofix K2.2.2/K₂CO₃ mixture of water and acetonitrile. After azeotropic drying of the solvent, the precursor F-PyTFP in a mixture of tert-butanol and acetonitrile (4:1) was added and heated at 40 °C for 15 min. The reaction mixture was diluted with acetonitrile (1 mL) and water (1 mL), and purified by semipreparative high performance liquid chromatography (HPLC) using a Nucleosil 100-7 C18 column (Machery-Nagel, Düren, Germany) as the stationary phase and 0.1% TFA/acetonitrile (25:75) as the mobile phase at a flow rate of 3 mL/min. The desired fraction (23–24 min, [¹⁸F]F-PyTFP) was collected, diluted with water (30 mL), and flushed through a C18 cartridge (Sep-Pak Light, Waters) to selectively retain [¹⁸F]F-PyTFP. Finally, the desired labeled specie was eluted with acetonitrile (1 mL). Radiochemical purity was determined by radio-HPLC using a Mediterranean C18 column (4.6 mm by 150 mm, 5 μ m) as a stationary phase and 0.1% TFA/acetonitrile as a mobile phase (0–1 min 25% acetonitrile; 1–9 min 25–90% acetonitrile; 9–12 min 90% acetonitrile; 12–13 min 90–25% acetonitrile; 13–15 min 25% acetonitrile) at a flow rate of 1.5 mL/min (retention time = 7.5 min).

Radiolabeling of nanomotors with [¹⁸F]F-PyTFP

¹⁸F-nanomotors were synthesized as reported elsewhere with minor modifications²⁵. Briefly, 400 μ L of nanomotor suspension (1 mg/mL) was centrifuged for 3 min at 2500 g, resuspended in 20 μ L of PBS (10 mM, pH 8), and incubated with 5 μ L of [¹⁸F]F-PyTFP in acetonitrile (50 \pm 2 MBq) at room temperature for 35 min. After incubation, the reaction mixture was diluted with 100 μ L of ultrapure water and purified by centrifugation (3 min, 2500 g, 3 washes). The pure labeled nanomotors were measured with a dose calibrator (CPCRC-25R, Capintec, Florham Park, NJ) and determined by radio-thin layer chromatography (radio-TLC) with iTLC-SG chromatography paper (Agilent Technologies, Santa Clara, CA), and methanol and dichloromethane (1/2) as the stationary and mobile phases, respectively. TLC plates were analyzed with a TLC-reader (MiniGITA, Elysia Raytest, Angleur, Belgium).

In vivo PET-CT imaging

For in vivo studies, we used C57BL/6J female mice (13 weeks old, Janvier Labs, *n* = 6). PET-CT imaging studies were carried out using MOLECUBES β and X-CUBE scanner (Molecubes, Gent, Belgium). Mice were anesthetized by inhalation of 3% isoflurane in pure O₂ and maintained by 1.5–2% isoflurane in 100% O₂. Under anesthesia of the animal in supine position, bladders were emptied by massaging the abdominal region. Immediately, animals were positioned on the PET scanner bed and ¹⁸F-nanomotors were introduced within the bladder with a catheter by intravesical administration using 200 mM of urea solution in water or ultrapure water as a vehicle (*n* = 3 per type of vehicle). After administration, 45-min whole-body PET imaging scans were performed, followed by CT acquisitions to obtain anatomical information. PET images were reconstructed by 3D-OSEM reconstruction algorithm and applying random, scatter, and attenuation corrections. PET and CT images of the same mouse were co-registered and analyzed by PMOD image processing tool. Two volumes of interests (VOIs) were placed on the upper and lower regions of the bladder (VOI 1 and VOI 2, respectively) to obtain the concentration of radioactivity over time. The resulting values were normalized to the maximum values obtained for each frame.

In vivo fluorescence imaging

Balb/c female mice were randomly divided into two groups (nanocomplex, nanomotor), which were anaesthetized by inhalation for the intravesical injection of fluorescence dye labeled samples into the bladders (50 μ L). After 30, 60, 90, and 120 min post-administration, the bladders were cut open to observe the bladder wall by depth. Then, the tissues were rinsed with PBS, flattened, and visualized with a two-photon microscope (FV1000, Olympus, Japan). The images were collected as Z-stacks (xyz, 400 Hz) at 512×512 pixels and analyzed with LAS AF Lite 2.6.1 of Leica. The 3D fluorescence images were rendered by Image J. At 12 h post-instillation, bladders were excised from euthanized mice and fixed in 4% paraformaldehyde for 48 h. The fixed bladders were embedded in paraffin blocks and 4 μ m thick sections were made for the measurement of fluorescence in bladder section. The sections were observed by optical microscopy.

In vivo clearance test and biochemical analysis

To test the clearance of nanomotor, Balb/c six female mice were divided into three groups ($n = 3$), which were treated by intravesical injection of fluorescent dye labeled STING, STNG@nanocomplex and STING@nanomotor. The amount of STING agonist was equivalent in each group by adjusting the fluorescent intensity of STING agonist. Fluorescence intensity was measured with a fluoro/lumino microplate reader (Fluoroskan Ascent FL, Thermo Fisher Scientific, Waltham, MA). Urine was extracted from the mice for 48 h to measure the fluorescent intensity of urine. After 48 h, whole blood and serum were collected for the hematological analyses to assess biochemical parameters, including MCV, RDW, HCT, HGB, MCH, MCHC, CREA, and BUN.

Murine bladder cancer model preparation

Eight weeks old female C57BL/6J mice were utilized for the preparation of bladder cancer model. MB49 cells were cultured in DMEM containing 10% FBS, 50 U/mL penicillin, and 50 mg/mL streptomycin at 37 °C under the humidified atmosphere of 5% CO₂. The mice were anesthetized, and the bladder was emptied with 24 G angiocath via urethral insertion. The bladder was wound by filling 100 μ L of 0.1 N HCl for 3 min to improve tumor cell implantation. MB49 cells of 1×10^6 suspended in 100 μ L of PBS was intravesically injected with 24 G angiocath through the urethra. Throughout the experiments, mice were monitored and weighed for health and welfare monitoring. The maximal thickness of the bladder tumor did not exceed 3 mm and all mice used in the experiments were euthanized just before bladder harvesting, according to the recommendations of the Institutional Animal Care and Use Committee.

Intravesical treatment of bladder cancer-bearing mice

To assess the antitumor effect and CD8 T cell infiltration to bladder cancer, drugs were intravesically injected on day 4 and 8 after bladder tumor cell instillation. The mice were euthanized 2 weeks after tumor cell instillation. To evaluate the cytokine production by each drug injection in bladder cancer, the drug was injected on day 7 after tumor cell instillation and the mice were euthanized 24 h later. The injected sample volumes and the concentrations on each day are described in the following: STING (10 μ g/100 μ L), nanomotor, STING@nanocomplex (10 μ g for STING/100 μ L), STING@nanomotor (10 μ g for STING/100 μ L) and same volume of PBS. To evaluate the antitumor effect of intravesical BCG therapy, 3×10^6 CFU/50 μ L of BCG was intravesically injected into urinary bladder on 4 and 8 d following the bladder tumor cell instillation. The tumor size was assessed two weeks after tumor cell instillation, comparing the control group and the STING@nanomotor treatment group. The antitumor effect of the anti-PD-1 antibody and its combinatorial effect was assessed in the MB49 bladder cancer model. A dose of 200 μ g/50 μ L of anti-PD-1 was injected intraperitoneally on days 4 and 8, along with intravesical treatment of either PBS or

STING@nanomotor. The tumor size was assessed two weeks after tumor cell instillation.

In vivo bioluminescence imaging

The FUGW-luc-eGFP vector was obtained from the Molecular Imaging and Neurovascular Research Laboratory at Dongguk University Ilsan Hospital (Goyang, Republic of Korea). FUGW-luciferase-eGFP expressing cells were produced as follows: the FUGW-luc-eGFP vector was transfected into the MB49 cell line (MB49-luc2). Cells incorporating FUGW-luc-eGFP were sorted using the GFP channel in a BD FACS Aria II (BD Biosciences, Franklin Lakes, NJ). The tumor model for the bioluminescence imaging was developed using MB49-luc cells. Mice were intraperitoneally injected with 150 mg/kg of D-luciferin (Promega, Madison) 5–10 min before imaging. They were then anesthetized in an induction chamber (2–3% isoflurane with oxygen) and placed in the imaging instrument. Bioimages were acquired using an IVIS Lumina SS imaging system on days 0, 2, 4, 7, 9, 11, and 14 following the tumor cell instillation. The region of interest (ROI) of the same size and shape was used for all acquired images to measure the total flux (photons per sec) in the ROI. Living Image software (Version 2.20, Xenogen, Alameda, CA) was used to quantify the signals emitted from the ROI.

Flow cytometry analysis

Harvested urinary bladder samples were digested with an enzyme buffer containing 2 mg/ml collagenase type2-II, 0.1 mg/ml DNase I, and 0.8 mg/ml Dispase at 37 °C for 30 min and filtered with a 40 μ m nylon mesh to remove cell clumps. ACK lysis buffer was added and incubated for 5 min at room temperature to remove RBCs. The single suspended cells were incubated in FACS buffer (5% bovine serum in PBS) with antibodies (1:200 dilution) including anti-mouse CD45, anti-mouse CD11c, anti-mouse CD80, anti-mouse CD86, anti-mouse MHC-II, anti-mouse CD45, anti-mouse CD3 epsilon, anti-mouse CD4, anti-mouse CD8a, anti-mouse CD4, anti-mouse CD25, anti-mouse CD11b, anti-mouse F4/80, MHC-II, anti-mouse CD11c. We analyzed the following cell subsets: (i) CD8⁺ T cells, gated as DAPI⁻/CD45⁺/CD3e⁺/CD4⁺/CD8a⁺ cells; (ii) CD4⁺ T cells, gated as DAPI⁻/CD45⁺/CD3e⁺/CD8a⁻/CD84⁺ cells; (iii) T_{reg} cells, gated as FVS450⁻/CD45⁺/CD4⁺/CD25⁺ (iv) Dendritic cells, gated as DAPI⁻/CD45⁺/CD11c⁺ cells; (v) TAMs, gated as DAPI⁻/CD45⁺/CD11b⁺/F4/80⁺ cells. The expression levels of CD80, CD86 and MHC-II on DC were presented as a mean value. The specific flow cytometry process was presented in Supplementary Fig. 17.

Histological analysis of bladder

For whole mount staining, bladder was filled with 1% agarose to prevent shrinkage before euthanized. The resected bladder was fixed in 4% paraformaldehyde in PBS for 8 h. For hematoxylin-eosin (H&E) and immunohistochemistry staining, samples were embedded in paraffin block after serial incubation with methyl benzoate and xylene for 30 min at room temperature. Paraffin blocks were cut in 5–10 μ m thickness. The sections were deparaffinized, antigen-retrieved, incubated with primary antibody (anti-CD8a antibody, 1:200 dilution), amplified with the chromogen for the signal, counterstained, and mounted for visualization according to the manufacturer's instruction (Ventana Benchmark XT Staining system). The images were acquired by Nikon ECLIPSE Ci-L plus microscopy.

Quantitative real-time RT-PCR

The manipulated bladder was resected and the whole bladder was minced to extract RNA from the tissue with a RNeasy plus mini kit (Qiagen, Hilden, Germany). Total RNA was reverse-transcribed into cDNA with a GoScriptTM reverse transcription kit (Promega, Madison, WI). Then, quantitative real-time PCR was conducted by using FastStart Sybr Green Master mix (Roche, Basel, Swiss) and QuantStudioTM 5 Real-Time PCR System (Applied BiosystemTM, Middlesex County, MA).

GAPDH was used as a reference gene. The PCR primer sequences are listed in Supplementary Table 1.

Statistical analysis

Statistical analysis was carried out via the student's *t*-test using the software of SigmaPlot14.5 (Systat Software Inc. San Jose, CA). The values for **P* < 0.05, ***P* < 0.01, ****P* < 0.005, and *****P* < 0.001 were considered statistically significant. Data are expressed as means ± standard deviation (SD) from several separate experiments.

Reporting summary

Further information on research design is available in the Nature Portfolio Reporting Summary linked to this article.

Data availability

All data that support the findings of this study are available in the paper or its Supplementary Information. Source data are provided with this paper.

References

- Cumberbatch, M. G. et al. Repeat transurethral resection in non-muscle-invasive bladder cancer: a systematic review. *Eur. Urol.* **73**, 925–933 (2018).
- Kamat, M. et al. Bladder cancer. *Lancet* **388**, 2796–2810 (2016).
- Tan, W. S., Rodney, S., Lamb, B., Feneley, M. & Kelly, J. Management of non-muscle invasive bladder cancer: a comprehensive analysis of guidelines from the United States, Europe and Asia. *Cancer Treat. Rev.* **47**, 22–31 (2016).
- Pettenati, C. & Ingersoll, M. A. Mechanisms of BCG immunotherapy and its outlook for bladder cancer. *Nat. Rev. Urol.* **15**, 615–625 (2018).
- Wołaczewicz, M. et al. Immunotherapy in bladder cancer: current methods and future perspectives. *Cancers* **12**, 1181 (2020).
- van Puffelen, J. H. et al. Trained immunity as a molecular mechanism for BCG immunotherapy in bladder cancer. *Nat. Rev. Urol.* **17**, 513–525 (2020).
- Audisio, A. et al. New perspectives in the medical treatment of non-muscle-invasive bladder cancer: immune checkpoint inhibitors and beyond. *Cells* **11**, 357 (2022).
- Chen, Q., Sun, L. & Chen, Z. J. Regulation and function of the cGAS–STING pathway of cytosolic DNA sensing. *Nat. Immunol.* **17**, 1142–1149 (2016).
- Decout, A., Katz, J. D., Venkatraman, S. & Ablasser, A. The cGAS–STING pathway as a therapeutic target in inflammatory diseases. *Nat. Rev. Immunol.* **21**, 548–569 (2021).
- Luo, M. et al. A STING-activating nanovaccine for cancer immunotherapy. *Nat. Nanotechnol.* **12**, 648–6554 (2017).
- Corrales, L. et al. The host STING pathway at the interface of cancer and immunity. *J. Clin. Invest.* **126**, 2404–2411 (2016).
- Lu, X. et al. Engineered PLGA microparticles for long-term, pulsatile release of STING agonist for cancer immunotherapy. *Sci. Transl. Med.* **12**, eaaz6606 (2020).
- Koshy, S. T., Cheung, A. S., Gu, L., Graveline, A. R. & Mooney, D. J. Liposomal delivery enhances immune activation by STING agonists for cancer immunotherapy. *Adv. Biosyst.* **1**, 1600013 (2017).
- Shae, D. et al. Endosomolytic polymersomes increase the activity of cyclic dinucleotide STING agonists to enhance cancer immunotherapy. *Nat. Nanotechnol.* **14**, 269–278 (2019).
- Dane, E. L. et al. STING agonist delivery by tumour-penetrating PEG-lipid nanodiscs primes robust anticancer immunity. *Nat. Mater.* **21**, 710–720 (2022).
- Choi, H., Yi, J., Cho, S. H. & Hahn, S. K. Multifunctional micro/nanomotors as an emerging platform for smart healthcare applications. *Biomater* **279**, 121201 (2021).
- Peng, F., Tu, Y. & Wilson, D. A. Micro/nanomotors towards in vivo application: cell, tissue and biofluid. *Chem. Soc. Rev.* **46**, 5289–5310 (2017).
- Wan, M., Li, T., Chen, H., Mao, C. & Shen, J. Biosafety, functionalities, and applications of biomedical micro/nanomotors. *Angew. Chem.* **60**, 13158–13176 (2021).
- Arqué, X., Patino, T. & Sánchez, S. Enzyme-powered micro- and nano-motors: key parameters for an application-oriented design. *Chem. Sci.* **13**, 9128–9146 (2022).
- Patiño, T., Arqué, X., Mestre, R., Palacios, L. & Sanchez, S. Fundamental aspects of enzyme-powered micro- and nanoswimmers. *Acc. Chem. Res.* **51**, 2662–2671 (2018).
- Yoan, H., Liu, X., Wang, L. & Ma, X. Fundamentals and applications of enzyme powered micro/nano-motors. *Bioact. Mater.* **6**, 1727–1749 (2021).
- Hortelao, A. C., Carrascosa, R., Cremaes, N. M., Patiño, T. & Sanchez, S. Targeting 3D bladder cancer spheroids with urease-powered nanomotor. *ACS Nano* **13**, 429–439 (2019).
- Choi, H., Cho, S. H. & Hahn, S. K. Urease-powered polydopamine nanomotors for intravesical therapy of bladder diseases. *ACS Nano* **14**, 6683–6692 (2020).
- Choi, H., Jeong, S. H., Kim, T. Y., Yi, J. & Hahn, S. K. Bioinspired urease-powered micromotor as an active oral drug delivery carrier in stomach. *Bioact. Mater.* **9**, 54–62 (2022).
- Hortelao, A. C. et al. Swarming behavior and in vivo monitoring of enzymatic nanomotors within the bladder. *Sci. Robot.* **6**, eabd2823 (2021).
- Xu, D. et al. Enzyme-powered liquid metal nanobots endowed with multiple biomedical functions. *ACS Nano* **15**, 11543–11554 (2021).
- Sogias, I. A., Williams, A. C. & Khutoryanskiy, V. V. Why is chitosan mucoadhesive? *Biomacromolecules* **9**, 1837–1842 (2008).
- Kutcherlapati, S. N. R., Yeole, N. & Jana, T. Urease immobilized polymer hydrogel: long-term stability and enhancement of enzymatic activity. *J. Coll. Interf. Sci.* **463**, 164–172 (2016).
- Zhang, J. et al. Safe and effective removal of urea by urease-immobilized, carboxyl-functionalized PES beads with good reusability and storage stability. *ACS Omega* **4**, 2853–2862 (2019).
- Garaiova, Z. et al. Cellular uptake of DNA-chitosan nanoparticles: the role of clathrin- and caveolae-mediated pathways. *Int. J. Biol. Macromol.* **51**, 1043–1051 (2012).
- Pereira, P. et al. siRNA inhibition of endocytic pathways to characterize the cellular uptake mechanisms of folate-functionalized glycol chitosan nanogels. *Mol. Pharmaceutics* **12**, 1970–1979 (2015).
- Song, S. et al. Engineering transient dynamics of artificial cells by stochastic distribution of enzymes. *Nat. Comm.* **12**, 6897 (2021).
- Patiño, T. et al. Influence of enzyme quantity and distribution on the self-propulsion of non-Janus urease-powered micromotors. *J. Am. Chem. Soc.* **140**, 7896–7903 (2018).
- Jin, D. & Zhang, L. Collective behaviors of magnetic active matter: recent progress toward reconfigurable, adaptive, and multi-functional swarming micro/nanorobots. *Acc. Chem. Res.* **55**, 98–109 (2022).
- Wang, J., Xiong, Z. & Tang, J. The encoding of light-driven micro/nanorobots: from single to swarming systems. *Adv. Intell. Syst.* **3**, 2000170 (2021).
- Yang, L. et al. Autonomous environment-adaptive microrobot swarm navigation enabled by deep learning-based real-time distribution planning. *Nat. Mach. Intell.* **4**, 480–493 (2022).
- Didden, N. On the formation of vortex rings: rolling-up and production of circulation. *J. Appl. Math. Phys. (ZAMP)*. **30**, 101–116 (1979).
- Joice, G. A., Bivalacqua, T. J. & Kates, M. Optimizing pharmacokinetics of intravesical chemotherapy for bladder cancer. *Nat. Rev. Urol.* **16**, 599–612 (2019).

39. Bauer, M., Wagner, C. C. & Langer, O. Microdosing studies in humans: the role of positron emission tomography. *Drugs R. D.* **9**, 73–81 (2008).
40. Bergstrom, M. The use of microdosing in the development of small organic and protein therapeutics. *J. Nucl. Med.* **58**, 1188–1195 (2017).
41. Ohkuri, T. et al. Effect of STING stimulation on macrophages: STING agonists polarize into “classically” or “alternatively” activated macrophages? *Hum. Vaccin Immunother.* **14**, 285–287 (2018).
42. Czapla, J. et al. Antitumor effect of anti-vascular therapy with STING agonist depends on the tumor microenvironment context. *Front. Oncol.* **13**, 1249524 (2023).
43. Nguyen, D. C. et al. Mannosylated STING agonist drugamers for dendritic cell-mediated cancer immunotherapy. *ACS Cent. Sci.* **10**, 666–675 (2024).
44. Garon, E. B. et al. Pembrolizumab for the treatment of non-small-cell lung cancer. *N. Engl. J. Med.* **372**, 2018–2028 (2015).
45. Schmid, P. et al. Pembrolizumab for early triple-negative breast cancer. *N. Engl. J. Med.* **382**, 810–821 (2020).
46. Choueiri, T. K. et al. Overall survival with adjuvant pembrolizumab in renal-cell carcinoma. *N. Engl. J. Med.* **390**, 1359–1371 (2024).
47. Tran, L., Xiao, J.-F., Agarwal, N., Duex, J. E. & Theodorescu, D. Advances in bladder cancer biology and therapy. *Nat. Rev. Cancer* **21**, 104–121 (2021).
48. Li, R. et al. Oncolytic adenoviral therapy plus pembrolizumab in BCG-unresponsive non-muscle-invasive bladder cancer: the phase 2 CORE-001 trial. *Nat. Med.* **30**, 2216–2223 (2024).
49. Kweon, D.-K., Song, S.-B. & Park, Y.-Y. Preparation of water-soluble chitosan/heparin complex and its application as wound healing accelerator. *Biomaterials* **24**, 1595–1601 (2003).
50. Choi, H. et al. Microalgae-based biohybrid microrobot for accelerated diabetic wound healing. *Small* **19**, 2204617 (2023).
51. Kim, K. S. et al. Noninvasive transdermal vaccination using hyaluronan nanocarriers and laser adjuvant. *Adv. Func. Mater.* **26**, 2512–2522 (2016).

Acknowledgements

This research was supported by the Basic Science Research Program (2020R1A2C3014070) (S.K.H.) and BRIDGE Research Program (2022M3C1C3095052) (S.K.H.) of the National Research Foundation (NRF) funded by the Ministry of Science and ICT, Korea. This research was also supported by the Korea Medical Device Development Fund grant (RS-2023-00253749) (S.K.H.) and the National Research Foundation of Korea (NRF) B-IRC grant (RS-2023-00260454) (S.K.H.) funded by the Korean government. This work was supported by the National Research Foundation of Korea (NRF) grant funded by Korea government, Basic Science Research Program (RS-2024-00460035) (H.C.) through the NRF funded by the Ministry of Education, Korea. The research leading to these results has also received funding from the European Research Council (ERC) under the European Union’s Horizon 2020 research and innovation programme (grant agreement 866348, i-NanoSwarms) (S.S.), “la Caixa” Foundation under the grant agreement LCF/PR/HR21/52410022 (BLADDEBOTS project) (S.S. and J.L.), the CERCA program by the Generalitat de Catalunya, the Secretaria

d’Universitats i Recerca del Departament d’Empresa i Coneixement de la Generalitat de Catalunya (S.S.), the “Centro de Excelencia Severo Ochoa”, funded by Agencia Estatal de Investigación (CEX2018-000789-S) (S.S.), and Grant PID2020-117656RB-I00 funded by MCIN/AEI/10.13039/501100011033 (J.L.).

Author contributions

H.C. and S.J. contributed equally to this work. S.K.H. and G.Y.K. conceived the idea. S.K.H., S.S., G.Y.K., J.L., and C.K. supervised the project, designed the experiment, and wrote the manuscript. H.C. and T.Y.K. performed all the in vitro experiments. H.C. and A.B. performed the simulation and analyzed the data. H.C., C.S., and H.S.L. performed in vivo experiments. H.C. and S.J. wrote the manuscript. All authors contributed to scientific discussion and editing of the manuscript.

Competing interests

The authors declare no competing interests.

Additional information

Supplementary information The online version contains supplementary material available at <https://doi.org/10.1038/s41467-024-54293-z>.

Correspondence and requests for materials should be addressed to Cheol Kwak, Gou Young Koh, Samuel Sánchez or Sei Kwang Hahn.

Peer review information *Nature Communications* thanks Cecilia Cabrera, Chun Mao, and the other, anonymous, reviewer(s) for their contribution to the peer review of this work. A peer review file is available.

Reprints and permissions information is available at <http://www.nature.com/reprints>

Publisher’s note Springer Nature remains neutral with regard to jurisdictional claims in published maps and institutional affiliations.

Open Access This article is licensed under a Creative Commons Attribution-NonCommercial-NoDerivatives 4.0 International License, which permits any non-commercial use, sharing, distribution and reproduction in any medium or format, as long as you give appropriate credit to the original author(s) and the source, provide a link to the Creative Commons licence, and indicate if you modified the licensed material. You do not have permission under this licence to share adapted material derived from this article or parts of it. The images or other third party material in this article are included in the article’s Creative Commons licence, unless indicated otherwise in a credit line to the material. If material is not included in the article’s Creative Commons licence and your intended use is not permitted by statutory regulation or exceeds the permitted use, you will need to obtain permission directly from the copyright holder. To view a copy of this licence, visit <http://creativecommons.org/licenses/by-nc-nd/4.0/>.

© The Author(s) 2024